Effects of scanning speed on mechanical, wear property, and corrosion behavior of CP-Ti fabricated by the selective laser melting technique

Weimin Chen [a*], Jinlong Hu [a,b], Zhuhao Wen [a], Haoqin Lin [a], Liying Sun [a*], Qiang Zhang [c]

[a] Institute of New Materials, Guangdong Academy of Sciences, National Engineering Research Center of Powder Metallurgy of Titanium & Rare Metals, Guangdong Provincial Key Laboratory of Metal Toughening Technology and Application, Guangzhou, Guangdong, China

[b] School of Materials Science and Engineering, Lanzhou Jiaotong University, Lanzhou, China
[c] Suzhou Laboratory, Suzhou, Jiangsu, China
[*]Corresponding author. *E–mail address*: chenweiming126@163.com; sunliying_48@163.com

(Received 03 September 2025; Accepted 06 April 2026)

Abstract

In this work, CP-Ti was prepared by the selective laser melting (SLM) technique to systematically explore the effect of scanning speed on microstructure, mechanical, wear properties, and corrosion behavior. The optimum relative density of 99.87±0.12% was obtained by using the scanning speed of 800 mm/s, while its tensile strength, yield strength, elongation, and hardness were 543±17 MPa, 453±7 MPa, 14±1%, and 294±4 HV, respectively. Moreover, SLM-processed CP-Ti with the optimum relative density had the lowest value of wear rate (2.72×10^{-7} mm^2/N) and excellent corrosion resistance. These results indicated that the CP-Ti with high relative density, strength and hardness, low wear rate, and excellent corrosion resistance could be fabricated by controlling the scanning speed, and further used for the biomedical implant applications well.

Keywords: Selective laser melting (SLM); CP-Ti; Scanning speed; Mechanical and wear properties; Corrosion behavior.

1 Introduction

Because of their excellent corrosion resistance, and excellent bio-compatibility, Ti and its alloys have become exceedingly significant in the fields of artificial hip, artificial knee joint, bone plate, and implants in recent years [1-4]. Therefore, CP-Ti and Ti-6Al-4V alloy are widely regarded and used as commercially metallic biomedical materials. However, the long-term use of Ti-6Al-4V may lead to several serious diseases, such as Alzheimer's disease, Parkinson's syndrome, and memory impairment,due to the release of Al and V ions from the alloy [5, 6].

With the development of addictive manufacturing technologies over the past decade, the preparation of some alloys like Ni-Ti alloy components has overcome many challenges posed by traditional machining methods [7]. Characterized by its high performance than other traditional preparation processes, Selective laser melting (SLM) has been used in many fields

[8]. Selective laser melting (SLM) technique can produce near-net parts with superb mechanical properties, excellent surface state, and numerous complex shapes [9, 10]. Being involved in casting and machining, it results in some issues like weak strength, metallurgical defects, and badness cutting performance in traditional manufacturing of CP-Ti. However, the high-energy laser beams invited in SLM processing facilitate a strikingly rapid cooling rate (10^3-10^8 K/s) [11] than other methods. This enables substantal grain refinement and even relatively high strength. Thus, the SLM technique has been widely used in the biomedical and aerospace industries [12-17].

The SLM technique has been used to prepare CP-Ti. Table 1 summaries the mechanical properties of CP-Ti fabricated using various techniques reported in Refs. [18-28].The purpose of this compilation is to define the scope of achievable properties and to underscore the research gap addressed in this work: the systematic investigation of scanning speed as an isolated variable. Zhang et al. [29] investigated the effects of scanning speed (ranging from 10 mm/s-200 mm/s) on the relative density and hardness of CP-Ti fabricated by their self-developed selective laser melting system. They reported that relative density decreased with increasing scanning speed, while hardness initially increased and then decreased as scanning speed increased. It should be noted that the relatively low scanning speeds employed in investigation [29] needs to be studied across a broader range of other speeds. Therefore, it is of significance to systematically explore the effects of scanning speed on the mechanical, wear, and corrosion properties of CP-Ti fabricated via the selective laser melting (SLM) technique.

Table 1. Summary of reported mechanical properties of CP-Ti under various conditions

Process	UTS (MPa)	YS (MPa)	ε (%)	HV	Reference
Cast (Grade 1)	240	170	24	-	[18]
Cast (Grade 2)	345	275	20	-	[18]
Cast (Grade 3)	450	380	18	-	[18]
Cast (Grade 4)	550	485	15	-	[18]
SLM (Grade 1)	512	422	18	228	[19]
LENS (Grade 1)	467	386	20	201	[19]
WAAM (Grade 1)	440	353	26	190	[19]
PM	576	450	9	190	[20]
SLM (Grade 2)	757	555	19	261	[21]
SLM (Grade 2)	650	500	19	-	[22]
SLM	1057	784	24	307	[23]
SLM (Grade 1)	800	721	12	185	[24]
SLM	714	533	18	224	[25]

SLM	592	461	21	209	[26]
SLM (Grade 1)	641	560	-	257	[27]
SLM (Grade 1)	-	502	34	-	[28]

In the table, the abbreviationsLENS, PM, and WAAM represent laser engineered net shaping, powder metallurgy, and wire arc additive manufacturing, respectively. This table is intended to illustrate the broad range of achievable properties and the significance of process history, not for direct numerical comparison.

In the present work, the SLM technique was invited to fabricate CP-Ti bulk (Grade 2), and the optimal parameters during the process of SLM were explored by continuously optimizing the parameters to achieve the high relative density. A systematic investigation was then conducted to examine the effects of scanning speed on the mechanical, wear, and corrosion properties of the SLM-processed CP-Ti. In addition, the fracture behavior and associatied wear mechanisms were also analyzed.

2 Experimental

2.1 Material, microstructure and the SLM processing

Argon gas atomization was used in preparing CP-Ti powder (Grade 2, supplied by Hebei Jiuyue New Material Technology Co., Ltd.). Fig. 1 shows the scanning electron microscopy (SEM) image of the morphology of CP-Ti powder by an ZEISS Gemini SEM 300 (ZEISS, Oberkochen, Germany). Fig. 2 shows the experimental workflow for fabricating samples via selective laser melting (SLM). CP-Ti specimens were fabricated by selective laser melting (SLM). The titanium powder was sieved and dried to ensure uniform particle size and low moisture content, and then uniformly spread on the building platform. A high-energy laser selectively melted the powder layer by layer according to the CAD model. After cooling, the as-printed samples were removed from the substrate and separated by wire electrical discharge machining to reduce thermal and mechanical damage and maintain material integrity. And the microstructure, tensile fracture morphology and wear scar morphology of SLM-processed CP-Ti with diverse scanning speeds were also observed by SEM. The phase of the CP-Ti was identified by X-ray diffraction (XRD) from an Ultima IV diffractometer (Rigaku, Tokyo, Japan) with monochromatic Cu Kα radiation. The particle size distribution of powder was measured using a laser particle size analyzer (LA-350, Horiba, France), yielding D10, D50, D90 values of 24 μm, 32 μm, and 45 μm, respectively. The SLM processing was carried out via an HBD-150 (HBD, Zhongshan, China) apparatus, which was equipped with a 500 W fiber laser and a spot of 30 micron in diameter under a high-purity argon atmosphere.

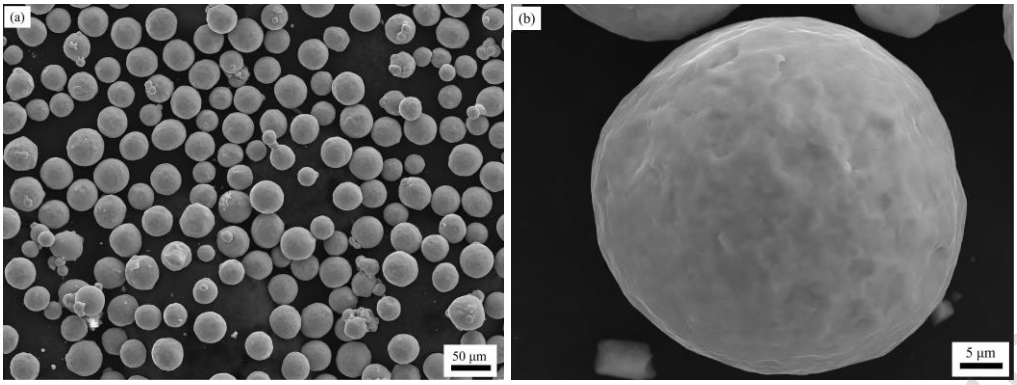

Fig. 1 Morphology of CP-Ti powder used in this work.

Cubic samples (10 mm ×10 mm ×10 mm) were fabricated at laser powers ranging from 120 W to 270 W and scanning speeds of 600 – 1000 mm/s. Meanwhile, following the work of Naeem Eshawish et al. [30], the layer thickness and hatching distance were kept constant at 30 μm and 120 μm, respectively, as these parameters were shown to yield optimal density in similar titanium alloys. Additionally, a continuous laser scanning mode was employed, utilizing a bar-like pattern with a 67 ° interlayer rotation angle, as also specified in [30]. To minimize the effect of the residual stress, the substrate was maintained at 80 ℃ throughout the entire SLM processing. Finally, relative density was determined by the Archimedes method.

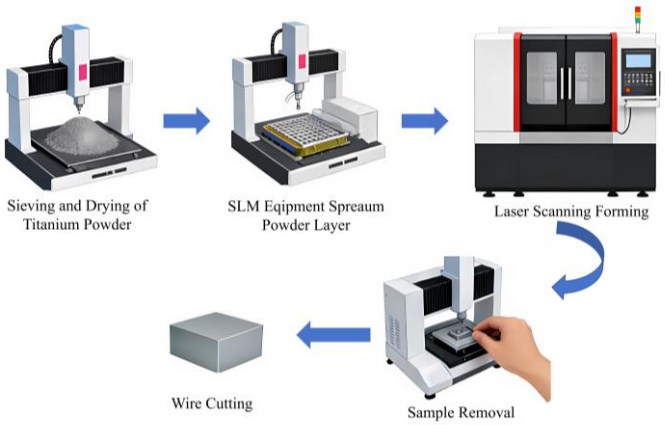

Fig. 2 The experimental workflow for fabricating samples via selective laser melting (SLM).

2.2 Mechanical property test

Equipped with an extensometer, a tensile testing machine (Instron 8802, Instron, USA) was invited to do tensile tests. The dog-bone-shaped tensile specimens, with a gauge length of 10 mm, a parallel length of 41 mm, and a thickness of 2 mm, were designed in compliance with GB/T 228.1-2010 and were subsequently sectioned from the SLM-fabricated blocks using wire electrical discharge machining. A detailed dimensional drawing is provided in Fig. 3. Surface of tensile samples were ground by SiC grinding paper up to 2500 grit to remove the heat-affected layers. Strain rate of 1×10^{-3} s^{-1} at room temperature kept constant during the tests, and each group was retested at least three times to ensure accuracy. Young's modulus was determined from the slope of the initial linear portion of the stress-strain curves. Vickers hardness tests were then performed on the polished surface using a microhardness tester (HXD-

1000TMC, Shanghai Taiming Optical Instrument Co., Ltd, China), with a load of 200 g and dwell time of 15 seconds. To ensure the accuracy, each of samples was measured at 20 different points and averaged.

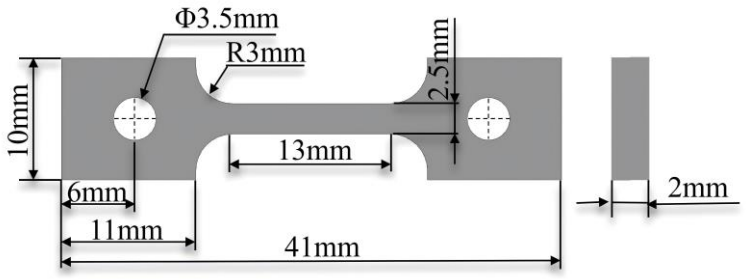

Fig. 3 The dimensions of the dog-bone-shaped tensile specimens employed in this work.

2.3 Wear test

Wear tests were performed on the SLM-processed CP-Ti with different scanning speeds under multi-functional tribometer (MFT-5000, Rtec-Instruments, Co., Ltd., USA). The tests were conducted under dry grinding conditions at room temperature for a duration of 1 hour, with an applied load of 2 N and a reciprocating frequency of 1 Hz. The friction pair is a zirconium ball of 5 mm in diameter. During the experiment, the friction coefficient was automatically generated by the software. And the wear rate was calculated by $Q= V/LF$ [31], where Q, V, L, and F represent the wear rate, wear volume loss, sliding distance, and applied load, respectively. The algorithm for the value L is the product of the sliding distance per second with the total time. Wear tests were performed three times on each sample and then averaged to ensure accuracy.

2.4 Electrochemical test

To investigate the corrosion behavior of SLM-processed CP-Ti with different scanning speeds in simulated body fluids (SBF), the electrochemical workstation (CHI 760, Chenhua, Shanghai, China) was introduced to do electrochemical test of a three-electrode system. This three-electrode system was primarily composed of the working electrode, reference electrode, and opposite electrode. In this work, the SLM-processed CP-Ti served as the working electrode, the saturated calomel electrode was used as the reference electrode, and the platinum electrode was regarded as the opposite electrode. To ensure surface quality, the samples with a working area of 1 cm^2 were sequentially ground using SiC papers up to a final grit of 2500. The tested samples should be immersed in simulated body fluids for 24 h at 37 ℃ to obtain a stable passivation film. Before the tests of potentiodynamic polarization and electrochemical impedance spectroscopy (EIS), open circuit potential (OCP) of all samples were executed in SBF to reach a stable potential. Potentiodynamic polarization tests were then conducted at a scanning rate of 1.0 mv/s from -1 V to 1 V, and the current density was calculated by the Tafel extrapolation method from the corresponding electrochemical potentiodynamic polarization curves. EIS was conducted with an alternating current amplitude of 10 mV over a frequency range from 10^5 Hz to 10^{-2} Hz.

2.5 Data Analysis and Presentation

All quantitative results in this study are derived from at least three independent

experimental replicates (n ≥ 3) to ensure statistical reliability. In the bar and line charts presented throughout this work: Data points or column heights represent the arithmetic mean. Error bars represent the standard deviation (SD), which quantifies the dispersion of the raw data and reflects the experimental reproducibility.The mean and standard deviation were calculated according to the following equations, respectively: $\bar{x} = \frac{1}{n}\sum_{i=1}^{n} x_i$ and $s=\sqrt{\frac{\sum_{i=1}^{n}(x_i-\bar{x})^2}{n-1}}$. Within them, x_i is an individual measurement and n is the sample size.

3 Results and discussion

3.1 Densification and microstructural characterization

The spherical or nearly spherical powder is shown in Fig. 1, indicating that it possesses excellent mobility. Some miniature CP-Ti particles are adhered to surface of larger ones as shown in Fig. 1(a), and the enlarged image in Fig. 1(b) clearly displays its spherical morphology. Fig. 4(a) shows the relative density of SLM-processed CP-Ti. The relative density falls below 99% under conditions where the scanning speed is below 700 mm/s and the laser power is less than the value of 170 W. Nevertheless, when the scanning speed is confined to 700 - 800 mm/s and the laser power to 170 - 220 W, the relative density surpasses 99%. Moreover, four samples have a relative density of over 99.5% (the yellow platform represents a relative density of 95% depicted in the figure). It is noteworthy that the SLM-processed CP-Ti, under the scanning speed of 800 mm/s and laser power of 270 W, has the highest relative density of 99.87±0.12%. And the variation of relative density for the SLM-processed samples with the constant laser power of 270 W is well significantly with the increasing scanning speed. Thus, the laser power was fixed at 270 W, and its effects were excluded to isolate and investigate the influence of scanning speed. Fig. 4(b) illustrates a diagram of the relationship between scanning speeds and relative density in the conditions with the laser power of 270 W, hatch distance of 120 μm, and layer thickness of 30 μm. Whilst, the laser energy density is a crucial factor to determine the relative density of samples fabricated by SLM, which is inversely proportional to the scanning speed [32]. Based on this relationship, a decrease in scanning speed leads to an increase in laser energy density. The higher energy density results in significant quantities of particles becoming molten and achieving a higher relative density. If the scanning speed continues to decrease (below 800 mm/s), the relative density would decrease again, due to the balling effect and dross formation appeared in the melt pool. As shown in Fig. 4(b), the relationship between relative density and scanning speed is nonlinear, consistent with the results reported in Ref. [33]. The minimum and maximum values of relative density are 94.24±0.34% and 99.87±0.12%, respectively.

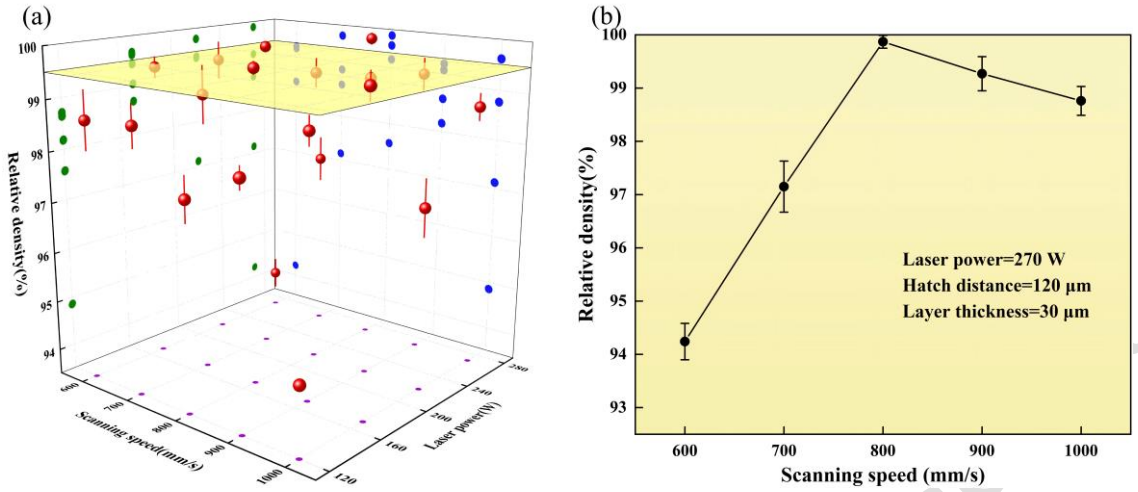

Fig. 4 (a) The relative density of CP-Ti by various SLM parameters. In the figure, purple, blue, and green denote the XY-, ZX-, and YZ-plane projections. (b) relationship between relative density and scanning speed when laser power, hatch distance, and layer thickness are 270 W, 120 μm, and 30 μm, respectively.

The microstructures of SLM-processed CP-Ti obtained at diverse scanning speeds are presented in Fig. 5. Defects such as gas pores and unmelted particles can be observed in the figure. Following Luo et al. [34], these gas pores are defined as keyholes, formed iprimarily due to the recoil pressure exerted on the molten pool. Large amounts of sparsely visible pores and unmelted particles are evident in the SEM image of the cross-section pdoduced at the relatively low scanning speed of 600 mm/s. As the scanning speed increases to 800 mm/s, the sample becomes nearly dense with minimal defects. While a reduction in porosity is observed with increasing speed up to 800 mm/s, a scanning speed of 1000 mm/s results in a notable increase in pores and irregular defects, evident in Fig. 5(e). Consequently, porosity progressively decreases as the scanning speed increases from 600 to 800 mm/s, reaching a minimum at 800 mm/s, and then increases again at 1000 mm/s. The SLM-processed CP-Ti with scanning speed of 800 mm/s has the highest relative density, which is consistent with the nearly dense microstructure shown in Fig. 5(c).

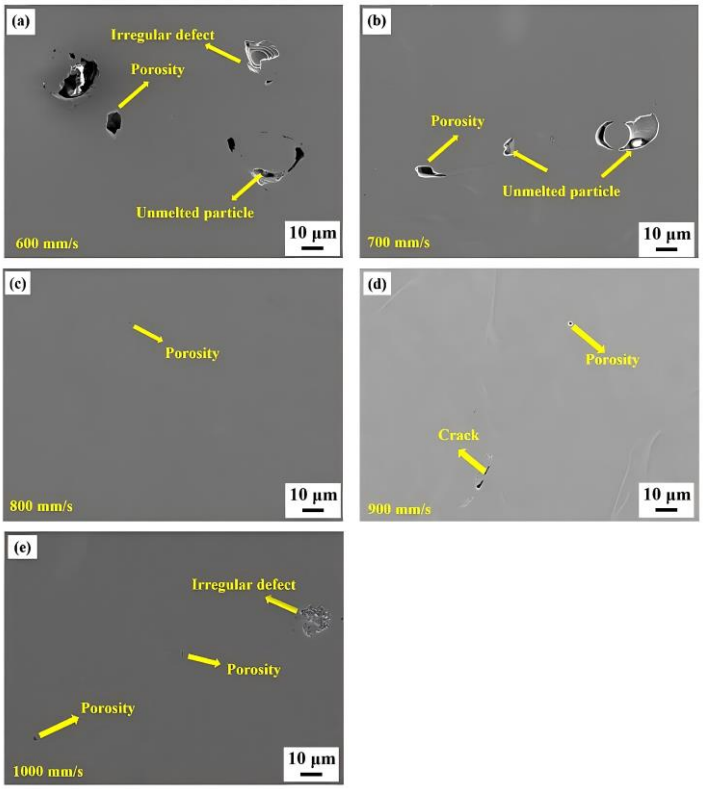

Fig. 5 Microstructure of SLM-processed CP-Ti with different scanning speeds: (a) 600 mm/s, (b) 700 mm/s, (c) 800 mm/s, (d) 900 mm/s, and (e) 1000 mm/s.

The XRD patterns of SLM-processed CP-Ti, acquired over a range of 20°-90°, are depicted in Fig. 6(a). The patterns indicate that the SLM-processed CP-Ti consists solely of a single α (hexagonal close-packed, hcp) phase, with no detectable peaks corresponding to rutile or anatase. Fig. 6(b) shows an enlarged section of the XRD patterns between 39.5°- 41°. Compared with the CP-Ti powder, the diffraction peak shifts to a lower angle in the SLM process sample, which is attributed to residual stress induced by the process [21], a finding consistent with the other studies [23].

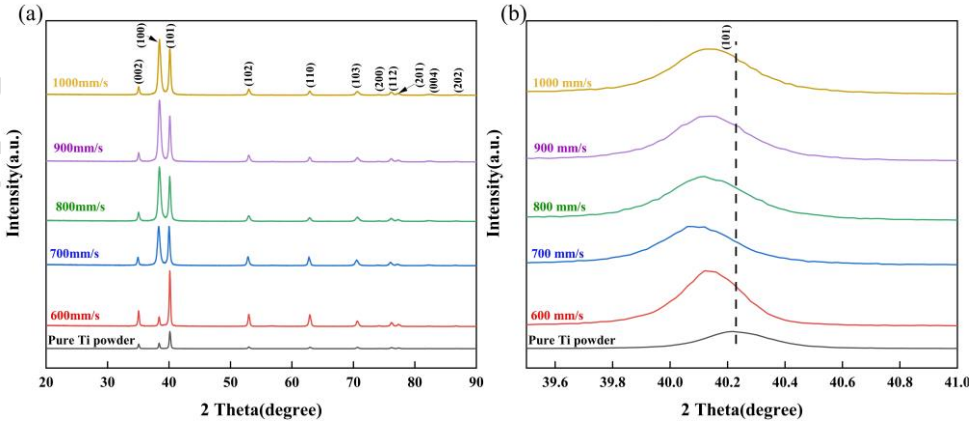

Fig. 5 XRD patterns of (a) CP-Ti powder and SLM-processed CP-Ti, (b) The enlarged area in the range of 39.5° - 41°.

3.2 Mechanical property

The microhardness of the SLM-processed CP-Ti, measured at different scanning speeds, is plotted as a function of speed in Fig. 7(a). It increases with scanning speed from 600 to 800 mm/s, reaching a maximum at 800 mm/s, and then decreases at 1000 mm/s. Notably, the microhardness peaks at 294.17±3.97 HV for the sample processed at 800 mm/s, constituting a 17.6% improvement over that at 600 mm/s. Moreover, it is 1.05 times higher than that of 1000 mm/s. Obviously, the variation of microhardness is similar to that of relative density, demonstrating that relative density is a key determinant of microhardness in this material. In addition, the hardness of CP-Ti in the as-cast state is 160 HV [35], which is 1.84 times lower than that of SLM-processed CP-Ti with the scanning speed of 800 mm/s. The tensile stress-strain curves of SLM-processed CP-Ti speciments obtained at different scanning speeds are presented in Fig. 7(b). The yield strength, tensile strength, elongation, and Young's modulus (E) of SLM-processed samples with different scanning speeds are presented in Table 2. The results indicate that the SLM-processed CP-Ti fabricated at a relatively low scanning speed of 600 mm/s exhibits an ultimate tensile strength of 402±5 MPa, a yield strength of 328 ± 10 MPa, and an elongation of 24±1%. As the scanning speed increases to 800 mm/s, the ultimate tensile strength increases to 543±17 MPa and yield strength raises to 453±7 MPa, while the ductility drops to 14±1 %. In contrast, at the higher scanning speed of 1000 mm/s, the elongation shows little variation, but both the tensile and yield strengths drop to 461±3 MPa and 385±2 MPa, respectively.Thus, the presently measured yield strength and tensile strength exhibit a consistent trend, which mirrors the variation in microhardness. Besides, the yield strength and tensile strength of as-cast CP-Ti [18] are 275 MPa and 345 MPa, respectively. Compared to the as-cast state, the SLM-processed CP-Ti at 800 mm/s exhibits 1.65 times higher yield strength and 1.57 times higher tensile strength. This enhancement is attributed primarily to the high cooling rate inherent to the SLM process [21]. The extremely high cooling rate leads to significant grain refinement, thereby resulting in enhanced strength according to the Hall-Petch relationship. Although residual stress is commonly present in SLM-processed samples due to the inherent nature of the process, it is not always detrimental to performance, as recent studies have indicated [36]. When high densification is guaranteed (here, the relative density of CP-Ti with scanning speed of 800 mm/s is 99.87%), retaining a controlled level of residual stress in the samples can significantly enhance the hardness and/or strength caused by the large number of dislocations [37].

Table 2 Mechanical results of SLM-processed CP-Ti with different scanning speeds

Scanning speed (mm/s)	YS (MPa)	UTS (MPa)	ε (%)	E (GPa)	δ (%)
600	327.78±9.67	402.29±5.16	24.04±1.21	108.77±0.89	0.275±0.002
700	368.41±6.04	444.80±3.24	11.83±2.4	107.75±2.65	0.307±0.003

800	452.63±7.06	542.67±16.51	13.96±0.74	109.48±0.82	0.378±0.002
900	425.18±0.92	497.18±4.09	13.12±2.67	108.77±0.89	0.358±0.002
1000	385.29±1.71	461.28±2.98	13.45±2.66	103.01±3.87	0.341±0.011

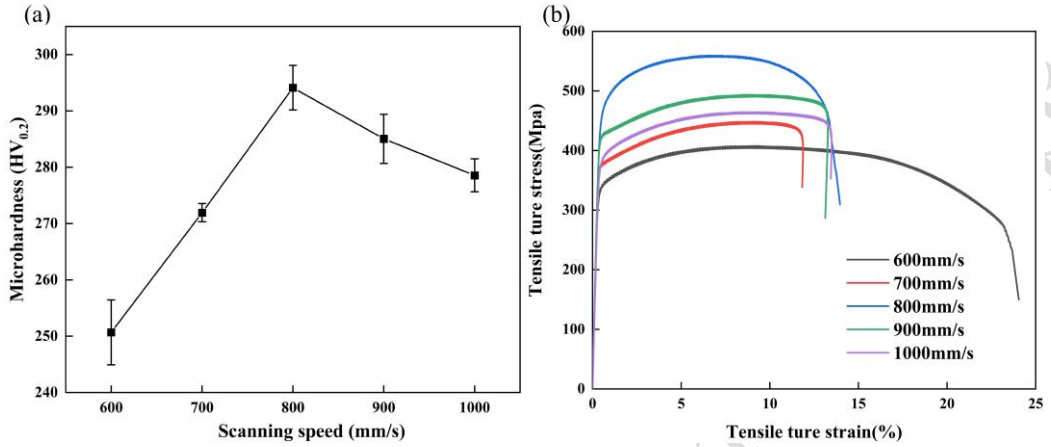

Fig.7 (a) Microhardness, (b) tensile stress-strain curves of the SLM-processed CP-Ti with different scanning speeds

Young's modulus is a vital indicator in the design and verification of biomedical materials, because modulus mismatch between the metallic implants and human bone can lead to the so-called stress shielding effect [38]. The Young's moduli of the samples exhibit minimal variation across different scanning speeds, as shown in Table 2, indicating that this parameter exerts negligible influence on the modulus. Generally, high strength or hardness coupled with low Young's modulus is exceedingly ideal for applications of orthopedic implants. The biomechanical compatibility of orthopedic implant materials is usually assessed by an elastic admissible strain δ, which is defined by dividing the yield strength YS by Young's modulus E ($\delta=YS/E$) [39, 40], which has been listed in Table 3. Larger elastic admissible strain demonstrates that this material is more suitable for biomedical applications. Evidently, the SLM-processed CP-Ti with scanning speed of 800 mm/s exhibits the highest elastic admissible strain, which is significantly higher than the 0.268% reported for as-cast CP-Ti in Ref. [18]. Hence, the SLM-processed CP-Ti has better biomechanical compatibility than the as-cast CP-Ti.

Resilience refers to the ability of the materials to release absorbed energy under the elastic deformation when stress is unloaded, which can be characterized by the elastic energy. On the other hand, toughness is defined as the total energy absorbed by a material per unit volume up to its point of fracture. The resilience of the material is usually characterized by the area of elastic region of stress-strain curve, and the area of stress-strain curve before ruptures is used to describe the toughness of the material [41]. Evidently, the sample processed at 800 mm/s possesses the highest elastic energy. Notably, the highest toughness is achieved at 600 mm/s, and comparable toughness is maintained at speeds of 800, 900, and 1000 mm/s.

3.3 Wear property

Fig. 8(a) shows the friction coefficient of SLM-processed CP-Ti. There is no significant variation on the SLM-processed CP-Ti in different scanning speeds. Fig. 8(b-c) displays the wear volume loss and wear rates for different scanning speeds. The wear rate exhibited by CP-Ti processed at 600 mm/s is 68.4% higher than that of the sample processed at 800 mm/s. Moreover, the wear rates of samples processed at 800 and 900 mm/s are comparable to each other and higher than that of the sample at 1000 mm/s. Both the wear volume loss and the wear rate show a similar trend of decreasing initially and then increasing as the scanning speed increases, with the minimum wear volume loss being achieved at a scanning speed of 800 mm/s. Although the friction coefficient does not vary in exact correspondence with the wear rate, and studies suggest no direct relationship between them, the coefficient primarily reflects the lubrication effect at the material interface. [42-44]. Fig. 8(d) illustrates the two-dimensional cross-section patterns of SLM-processed CP-Ti with different scanning speeds. A low wear rate corresponds to a wear scar with reduced depth and width. Hence, the variations in wear depth also verify the point that SLM-processed CP-Ti with a scanning speed of 800 mm/s exhibits the highest wear resistance.

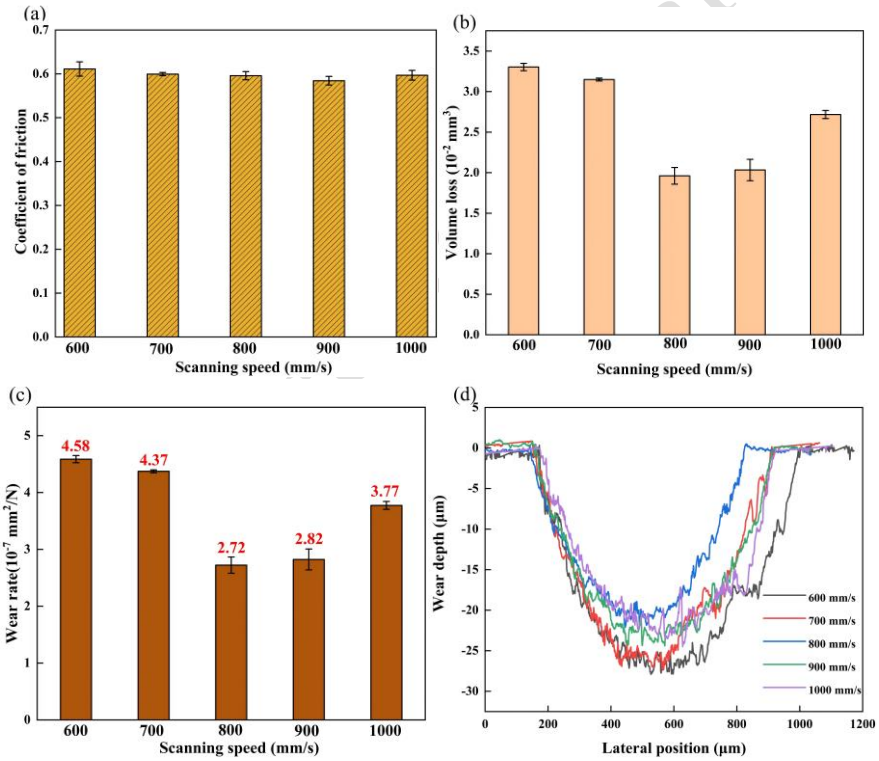

Fig. 8 (a) Friction coefficient, (b) wear volume loss, (c) wear rate and (d) the two-dimensional cross sections of SLM-processed samples after the wear tests

Fig. 9 shows the room-temperature wear scar morphology of SLM-processed samples. All samples exhibit similar wear scar morphologies, including obvious ploughing grooves, microcracks, delamination, and adhesive wear. These features, common to titanium alloys, arise from the severe plastic deformation and stress during sliding contact, given their nearly identical elemental composition. Ploughing grooves paralleled to sliding direction can be seen on the surface, which is considered as the typical feature of abrasive wear [45]. During sliding, the junctions are sheared, resulting in separation from one surface and attachment to the other.

This is a typical adhesion morphology, indicating that there is also an adhesive wear mechanism [46]. The main wear mechanisms in this work are adhesive wear and abrasive wear.

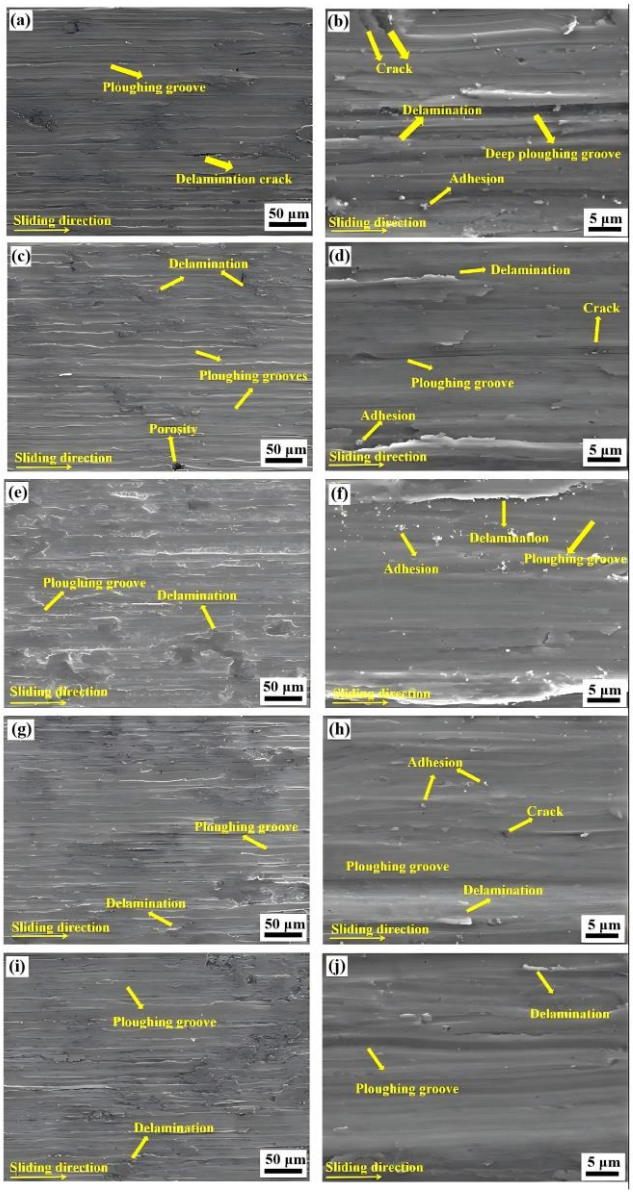

Fig. 9 Wear scar morphology of the SLM-processed CP-Ti with the scanning speeds: (a) (b) 600 mm/s, (c) (d) 700 mm/s, (e) (f) 800 mm/s, (g) (h) 900mm/s, and (i) (j) 1000 mm/s.

Wear resistance is not the inherent property, however, many factors could affect the wear resistance of samples, including hardness, roughness of wear surface, lubrication and temperature .etc. In this study, the samples underwent a dry sliding process against the ZrO_2 ball at room temperature. According to the Archard's wear law [47], wear resistance of the material is proportional to the corresponding hardness value. Thus, increased hardness improves the material's resistance to compression deformation, thereby enhancing its wear resistance. Fig. 10 shows the relationship of scanning speed, microhardness, and wear rate. Obviously, the wear rate is inversely proportional to hardness. It can be concluded that the wear resistance of CP-Ti processed at 800 mm/s is superior to that of the sample processed at 600

mm/s. This is due to the higher hardness of the former. Besides, SLM-processed CP-Ti samples with low strength and/or hardness would produce deeper ploughing grooves during plastic deformation. As vividly shown in the Fig. 7(a), the lowest hardness is reached with the low scanning speed of 600 mm/s. The depth of the ploughing grooves in Fig. 9(a-b) is the greatest, an observation consistent with the explanation provided above.

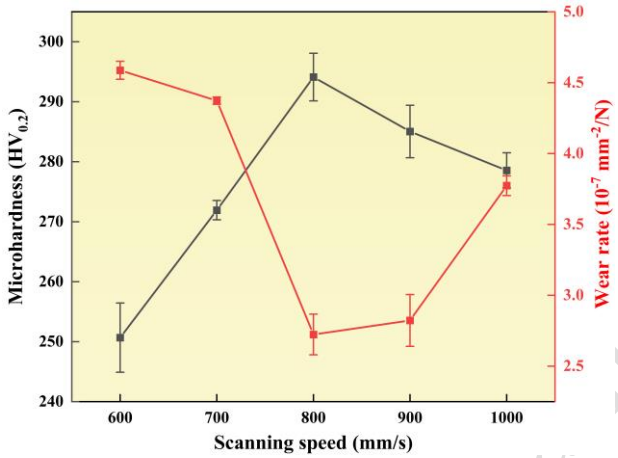

Fig. 10 The relationship among scanning speed, microhardness, and wear rate.

3.4 Corrosion behavior

The OCP values are measured in SBF solution for 3600 s to obtain the stable passive film. Following the OCP measurements, potentiodynamic polarization tests were conducted on the SLM-processed samples at different scanning speeds. The resulting curves are presented in Fig. 11(a). In the anodic region, the large stable passivation region can be seen in all the polarization curves, indicating that a stable passive film has been formed on the surface. Moreover, the passive film formed on CP Ti contains Ti^{2+}, Ti^{3+} and Ti^{4+} was found in Ref. [48]. The corrosion behavior of metallic materials is critically influenced by alloy composition, relative density, and phase structure. Since the composition and phase structure are kept stable for all SLM-processed CP-Ti, the crucial factor in this work is the relative density. Blackwood et al. [49] have proven that materials with the lower relative density are more prone to corrosion attack due to their greater true surface area exposed to the electrolyte. The corrosion current density (I_{corr}) and corrosion potential (E_{corr}) are obtained and listed in Table 3, which are generally used to evaluate the corrosion resistance [50]. The SLM-processed CP-Ti fabricated at 800 mm/s exhibits the lowest corrosion current density, corresponding to the highest corrosion resistance. Moreover, a scanning speed of 600 mm/s yields the highest I_{corr} value, which is 11.71 times that of the sample produced at 800 mm/s. When the scanning speed increases to 1000 mm/s, the Icorr value rises, becoming 193.5% higher than the optimal value achieved at 800 mm/s. As listed in the table, the I_{corr} values for SLM-processed CP-Ti increase in the order: S3 < S4 < S5 < S2 < S1, where S1–S5 denote scanning speeds of 600, 700, 800, 900, and 1000 mm/s, respectively. This result is in accordance with the variation of relative density.

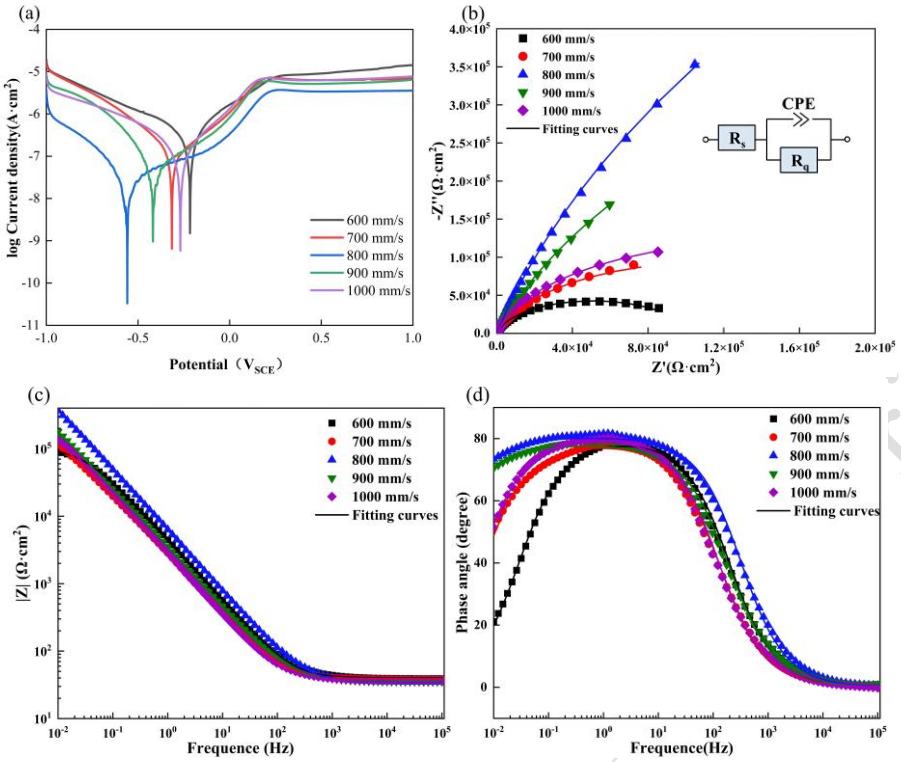

Fig. 11 Potentiodynamic polarization curves and EIS diagrams of SLM-processed CP-Ti in the SBF solution at 37℃: (a) Tafel curves; (b) Nyquist plots, (c) Bode magnitude plots, and (d) Bode phase plots

Table. 3 Electrochemical data obtained from electrochemical tests and fitting results.

Scanning speed (mm/s)	E_{corr} (V vs.SCE)	I_{corr} (μA·cm^{-2})	R_S (Ω·cm^2)	$CPE\times10^{-5}$ (F·cm^2)	$R_q\times10^5$ (Ω·cm^2)	n
600	-0.179±0.036	0.363±0.100	37.51±2.57	4.62±0.13	0.725±0.296	0.884±0.002
700	-0.260±0.054	0.171±0.016	38.43±0.46	5.42±1.97	1.94±0.357	0.887±0.016
800	-0.533± .025	0.031±0.001	37.47±1.99	3.93±0.81	20.281±3.72	0.901± 0.060
900	-0.371±0.048	0.065±0.003	35.43±0.65	4.46±1.41	10.059±3.361	0.885±0.018
1000	-0.268±0.001	0.091±0.002	38.91±1.46	6.49±0.45	2.911±0.053	0.887±0.002

To further explore the corrosion behavior and passivation mechanism of SLM-processed CP-Ti, EIS tests are performed in SBF solution at 37 ˚C. Nyquist and Bode plots of the impedance spectrum are shown in Fig. 11(b-d). In Fig. 11(b), all the samples show a semi-

circular characteristic, indicating a similar passivation mechanism. The largest diameter of the capacitive semicircle in the Nyquist plot, observed for the sample processed at 800 mm/s, corresponds to its highest corrosion resistance. In the Bode plots of Fig. 11(c), in the range of 10^4-10^3 Hz, the impedance of all the samples keeps constant, corresponding to the electrolyte resistance. Slope of impedance spectrum is nearly close to -1 when the frequency is below 10^2 Hz, indicating a typical feature of a single layer [51]. Ranking of impedance values Z at the terminate frequency (|Z| at 10^{-2} Hz) is given as follows: Z3 > Z4 > Z5 > Z2 > Z1, which is consistent with the polarization results. And the best corrosion resistant is found for CP-Ti with scanning speed of 800 mm/s. Besides, a simple equivalent circuit model, composed of R_S (*CPE*, R_q), was employed to fit the EIS data, as shown in the inset of Fig. 11(b). Here, R_S and *Rq* represent the electrolyte resistance and resistance of the passivation film, respectively. And the fitting results are shown in Table 3. The value of R_q can be also used as a corrosion behavior indicator, i.e. higher value R_q means better corrosion resistance. SLM-processed CP-Ti with scanning speed of 800 mm/s has the highest R_q value of $20.281\pm3.72\times10^5$ $\Omega\cdot cm^2$, indicting its great corrosion resistance. Consequently, the corrosion resistance of SLM-processed CP-Ti shows a non-monotonic dependence on scanning speed, peaking at 800 mm/s and degrading at both lower (600, 700 mm/s) and higher (900, 1000 mm/s) speeds.

4 Conclusions

In this work, CP-Ti was fabricated by SLM technique and then investigated from the aspects of microstructure, mechanical properties, wear and corrosion behaviors. Main conclusions are obtained as follows:

1) The relative density increasing first and then decreasing with the increasing of scanning speed. Moreover, XRD patterns showed that SLM-processed CP-Ti has a single α phase, and its peak position shifted towards to a lower angle due to the existence of residual stress.

2) Optimum mechanical property of SLM-processed CP-Ti is obtained by fixing the scanning speed of 800 mm/s, which includes microhardness of 294±4 HV, Young's modulus of 109±1 GPa, elongation of 14±1%, yield strength of 453±7 MPa, and tensile strength of 543± 17 MPa. And, the mechanical property is mainly related to relative density. Fracture mechanism of SLM-processed CP-Ti is ductile fracture. High elastic admissible strain also indicates that SLM-processed CP-Ti with the scanning speed of 800 mm/s is very suitable as a biomedical metallic implant.

3) Wear property and corrosion behavior are mainly depended on surface hardness and exposed true surface area, respectively. Therefore, the wear and corrosion rates which are positive correlation to the relative density increase first and then decrease with the increasing scanning speed. The main wear mechanisms of SLM-processed CP-Ti are adhesive wear and abrasive wear. SLM-processed CP-Ti with scanning speed of 800 mm/s has excellent wear and corrosion resistance for biomedical applications.

Acknowledgements

The authors gratefully acknowledge the financial supports from the Advanced Materials-National Science and Technology Major Project (Grant No. 2025ZD0619700), Guangdong Basic and Applied Basic Research Foundation, National Natural Science Foundation for Youth of China (Grant No. 51701083), GDAS' Project of Science and Technology Development

(Grant Nos. 2022GDASZH-2022010103 and 2022GDASZH-2022010107), GINM' Special Project of Science and Technology Development (Grant Nos. 2023GINMZX-202301020110 and 2023GINMZX-202301020102), and Evaluation Project of Guangdong Provincial Key Laboratory (Grant No. 2023B1212060043).

Author's Contributions

Weimin Chen: Conceptualization, Data curation, Formal analysis, Funding acquisition, Investigation, Writing – original draft. Jinlong Hu: Data curation, Formal analysis, Investigation. Zhuhao Wen: Data curation, Formal analysis, Investigation. Haoqin Lin: Data curation, Formal analysis, Investigation. Liying Sun: Formal analysis, Formal analysis, Investigation. Qiang Zhang: Formal analysis, Investigation.

Data availability Statement

Data will be made available on request.

Declarations of Interest

The authors declare that they have no known competing financial interests or personal relationships those could have appeared to influence the work reported in this paper.

References

[1] J. Ling, W. Chen, Y. Sheng, et al. A MGI-oriented investigation of the Young's modulus and its application to the development of a novel Ti–Nb–Zr–Cr bio-alloy, Materials Science and Engineering: C, 106, (2020) 110265. https://doi.org/10.1016/j.msec.2019.110265.

[2] H. Lin, G. Zhang, W. Chen, et al. Design of new β-type Ti alloys with outstanding corrosion and wear resistance for dental application, Corrosion Science, 241 (2024) 112520. https://doi.org/10.1016/j.corsci.2024.112520.

[3] W. Chen, J. Ling, K. Bai, et al. High-throughput studies and machine learning for design of β titanium alloys with optimum properties, Transactions of Nonferrous Metals Society of China, 34 (10) (2024) 3194–3207. https://doi.org/10.1016/S1003-6326(24)66602-1.

[4] K. Zhou, X. Yang, Y. An, et al. A review on advances of high-throughput experimental technology for titanium alloys, Transactions of Nonferrous Metals Society of China, 34 (11) (2024) 3425–3451. https://doi.org/10.1016/S1003-6326(24)66618-5.

[5] Y. Okazaki, S. Rao, and S. Asao. Effects of Ti, Al and V concentrations on cell viability, Materials Transactions, 39 (10) (1998) 1053–1062. https://doi.org/10.2320/matertrans1989.39.1053.

[6] J. Ling, D. Huang, K. Bai, et al. High-throughput development and applications of the compositional mechanical property map of the β titanium alloys, Journal of Materials Science & Technology, 71 (2021) 201–210. https://doi.org/10.1016/j.jmst.2020.07.035.

[7] Wang J, He D, Wu X, et al. Characterization of pre-alloyed NiTi powders produced by electrode induction-melting inert gas atomization for additive manufacturing. Journal of Mining and Metallurgy, Section B: Metallurgy, 58 (2) (2022) 219-228. https://doi.org/10.2298/JMMB211019006W.

[8] X. Huang, Y. T. Zhu, W. D. Huang, S. S. Qin, L. Wang, Microstructure evolution and mechanical properties of TiB/Ti6Al4V composites based on selective laser melting, Journal of Mining and Metallurgy B:Metallurgy, 58 (3) (2022) 439-450. https://doi.org/10.2298/JMMB220422025H.

[9] B.G.Y. Kumar, R.L. Kumar, R.V. Vignesh, et al. Microstructural evolution and bio-corrosion characteristics of cold-rolled Ti–6Al–4V alloy fabricated through selective laser melting for implant applications, JOM, 76 (10) (2024) 5958–5980. https://doi-org-s-348.libdb.csu.edu.cn/10.1007/s11837-024-06810-0.
[10] X. Zhang, R. Li, Y. Ma, et al. Effects of hot isostatic pressing on the microstructure and mechanical properties of K418 alloys fabricated by selective laser melting, JOM, 76 (11) (2024) 6240–6251. https://doi.org/10.1007/s11837-024-06765-2.
[11] M. Das, V.K. Balla, D. Basu, et al. Laser processing of SiC-particle-reinforced coating on titanium, Scripta Materialia, 63 (4) (2010) 438–441. https://doi.org/10.1016/j.scriptamat.2010.04.044.
[12] L.C. Zhang, and H. Attar. Selective laser melting of titanium alloys and titanium matrix composites for biomedical applications: A review, Advanced Engineering Materials, 18 (2016) 463–475. https://doi.org/10.1002/adem.201500419.
[13] I. Yadroitsev, P. Krakhmalev, and I. Yadroitsava. Selective laser melting of Ti6Al4V alloy for biomedical applications: Temperature monitoring and microstructural evolution, Journal of Alloys and Compounds, 583 (2014) 404–409. https://doi.org/10.1016/j.jallcom.2013.08.183.
[14] E. Fereiduni, A. Ghasemi, and M. Elbestawi. Selective laser melting of aluminum and titanium matrix composites: Recent progress and potential applications in the aerospace industry, Aerospace, 7 (6) (2020) 77. https://doi.org/10.3390/aerospace7060077.
[15] Y. Song, Y. Yan, R. Zhang, et al. Manufacture of the die of an automobile deck part based on rapid prototyping and rapid tooling technology, Journal of Materials Processing Technology, 120 (2002) 237–242. https://doi.org/10.1016/S0924-0136(01)01165-7.
[16] F. Klocke, A. Klink, D. Veselovac, et al. Turbomachinery component manufacture by application of electrochemical, electro-physical and photonic processes, CIRP Annals, 63 (2014) 703–726. https://doi.org/10.1016/j.cirp.2014.05.004.
[17] N. Lebaal, Y. Zhang, F. Demoly, et al. Optimised lattice structure configuration for additive manufacturing, CIRP Annals, 68 (2019) 117–120. https://doi.org/10.1016/j.cirp.2019.04.054.
[18] M. Niinomi. Mechanical properties of biomedical titanium alloys, Materials Science and Engineering: A, 243 (1998) 231–236. https://doi.org/10.1016/S0921-5093(97)00806-X.
[19] H. Attar, M.J. Bermingham, S. Ehtemam-Haghighi, et al. Evaluation of the mechanical and wear properties of titanium produced by three different additive manufacturing methods for biomedical application, Materials Science and Engineering: A, 760 (2019) 339–345. https://doi.org/10.1016/j.msea.2019.06.024.
[20] L. Bolzoni, E.M. Ruiz-Navas, and E. Gordo. Quantifying the properties of low-cost powder metallurgy titanium alloys, Materials Science and Engineering: A, 683 (2017) 47–53. https://doi.org/10.1016/j.msea.2017.01.049.
[21] H. Attar, M. Calin, L.C. Zhang, et al. Manufacture by selective laser melting and mechanical behavior of commercially pure titanium, Materials Science and Engineering: A, 593 (2014) 170–177. https://doi.org/10.1016/j.msea.2013.11.038.
[22] A. Barbas, A.S. Bonnet, P. Lipinski, et al. Development and mechanical characterization of porous titanium bone substitutes, Journal of the Mechanical Behavior of Biomedical

Materials, 9 (2012) 34–44. https://doi.org/10.1016/j.jmbbm.2012.01.008.
[23] Y.P. Dong, J.C. Tang, D.W. Wang, et al. Additive manufacturing of pure Ti with superior mechanical performance, low cost, and biocompatibility for potential replacement of Ti–6Al–4V, Materials & Design, 196 (2020) 109142. https://doi.org/10.1016/j.matdes.2020.109142.
[24] Q. Wang, K. Zhang, D. Qiu, et al. Additive manufacturing of high-strength commercially pure titanium through lanthanum oxide addition, Materials Characterization, 176 (2021) 111074. https://doi.org/10.1016/j.matchar.2021.111074.
[25] D.W. Wang, Y.H. Zhou, J. Shen, et al. Selective laser melting under the reactive atmosphere: A convenient and efficient approach to fabricate ultrahigh strength commercially pure titanium without sacrificing ductility, Materials Science and Engineering: A, 762 (2019) 138078. https://doi.org/10.1016/j.msea.2019.138078.
[26] E. Chlebus, B. Kuźnicka, R. Dziedzic, et al. Titanium alloyed with rhenium by selective laser melting, Materials Science and Engineering: A, 620 (2015) 155–163. https://doi.org/10.1016/j.msea.2014.10.021.
[27] D. Zhao, C. Han, Y. Li, et al. Improvement on mechanical properties and corrosion resistance of titanium-tantalum alloys in-situ fabricated via selective laser melting, Journal of Alloys and Compounds, 804 (2019) 288–298. https://doi.org/10.1016/j.jallcom.2019.06.307.
[28] J. Zhang, Y. Liu, M. Bayat, et al. Achieving high ductility in a selectively laser melted commercial pure-titanium via in-situ grain refinement, Scripta Materialia, 191 (2021) 155–160. https://doi.org/10.1016/j.scriptamat.2020.09.023.
[29] B. Zhang, H. Liao, and C. Coddet. Selective laser melting commercially pure Ti under vacuum, Vacuum, 95 (2013) 25–29. https://doi.org/10.1016/j.vacuum.2013.02.003.
[30] Eshawish N, Malinov S, Sha W, et al.Microstructure and mechanical properties of Ti-6Al-4V manufactured by selective laser melting after stress relieving, hot isostatic pressing treatment, and post-heat treatment, Journal of Materials Engineering and Performance, 30 (2021) 5290 – 5296. https://doi.org/10.1007/s11665-021-05753-w.
[31] X. Zhao, H. Liu, S. Li, et al. Combined effect of TiN coating and surface texture on corrosion-wear behavior of selective laser melted CP-titanium in simulated body fluid, Journal of Alloys and Compounds, 816 (2020) 152667. https://doi.org/10.1016/j.jallcom.2019.152667.
[32] J. Chen, X. Liao, J. Shu, et al. Microstructure tailoring of Ti–15Mo alloy fabricated by selective laser melting with high strength and ductility, Materials Science and Engineering: A, 826 (2021) 141962. https://doi.org/10.1016/j.msea.2021.141962.
[33] L.C. Zhang, D. Klemm, J. Eckert, et al. Manufacture by selective laser melting and mechanical behavior of a biomedical Ti–24Nb–4Zr–8Sn alloy, Scripta Materialia, 65 (2011) 21–24. https://doi.org/10.1016/j.scriptamat.2011.03.024.
[34] X. Luo, C. Yang, Z.Q. Fu, et al. Achieving ultrahigh-strength in beta-type titanium alloy by controlling the melt pool mode in selective laser melting, Materials Science and Engineering: A, 823 (2021). https://doi.org/10.1016/j.msea.2021.141731.
[35] B.W. Ho, C.P. Ju, and J.H. Chern Lin. Structure and properties of cast binary Ti–Mo alloys, Biomaterials 20 (22) (1999) 2115–2122. https://doi.org/10.1016/S0142-9612(99)00114-3.
[36] D. Wang, S. Wu, Y. Yang, et al. The effect of a scanning strategy on the residual stress of

316L steel parts fabricated by selective laser melting (SLM), Materials, 11 (2018) 1821. https://doi.org/10.3390/ma11101821.
[37] Y.H. Zhou, W.P. Li, D.W. Wang, et al. Selective laser melting enabled additive manufacturing of Ti–22Al–25Nb intermetallic: Excellent combination of strength and ductility, and unique microstructural features associated, Acta Materialia, 173 (2019) 117–129. https://doi.org/10.1016/j.actamat.2019.05.008.
[38] Z. Wen, Y. Wang, J. Ling, et al. High-throughput determination of the composition-dependent mechanical and diffusion properties in β Ti–Nb–Zr–Hf refractory alloys, Journal of Alloys and Compounds, 876 (2021) 160150. https://doi.org/10.1016/j.jallcom.2021.160150.
[39] S. Ozan, J. Lin, Y. Li, et al. Development of Ti–Nb–Zr alloys with high elastic admissible strain for temporary orthopedic devices, Acta Biomaterialia, 20 (2015) 176–187. https://doi.org/10.1016/j.actbio.2015.03.023.
[40] A.-H.M. Gepreel, and M. Niinomi. Biocompatibility of Ti-alloys for long-term implantation, Journal of the Mechanical Behavior of Biomedical Materials, 20 (2013) 407–415. https://doi.org/10.1016/j.jmbbm.2012.11.014.
[41] S. Ozan, J. Lin, W. Weng, et al. Effect of thermomechanical treatment on the mechanical and microstructural evolution of a β-type Ti–40.7Zr–24.8Nb alloy, Bioactive Materials, 4 (2019) 303–311. https://doi.org/10.1016/j.bioactmat.2019.10.007.
[42] N. Hua, X. Hong, L. Lin, et al. Mechanical, corrosion, and wear performances of a biocompatible Ti-based glassy alloy, Journal of Non-Crystalline Solids, 543 (2020) 120116. https://doi.org/10.1016/j.jnoncrysol.2020.120116.
[43] N. Hua, W. Chen, Q. Wang, et al. Tribocorrosion behaviors of a biodegradable $Mg_{65}Zn_{30}Ca_5$ bulk metallic glass for potential biomedical implant applications, Journal of Alloys and Compounds, 745 (2018) 111–120. https://doi.org/10.1016/j.jallcom.2018.02.138.
[44] Z. Liao, N. Hua, W. Chen, et al. Correlations between the wear resistance and properties of bulk metallic glasses, Intermetallics, 93 (2018) 290–298. https://doi.org/10.1016/j.intermet.2017.10.008.
[45] Z. Li, W. Lai, X. Tong, et al. Design of TiZrNbTa multi-principal element alloys with outstanding mechanical properties and wear resistance, Materials Science and Engineering: A, 845 (2022) 143203. https://doi.org/10.1016/j.msea.2022.143203.
[46] X. Yang, and C.R. Hutchinson. Corrosion-wear of β-Ti alloy TMZF (Ti–12Mo–6Zr–2Fe) in simulated body fluid, Acta Biomaterialia, 42 (2016) 429–439. https://doi.org/10.1016/j.actbio.2016.07.008.
[47] J. Lin, X. Tong, Z. Shi, et al. A biodegradable Zn–1Cu–0.1Ti alloy with antibacterial properties for orthopedic applications, Acta Biomaterialia, 106 (2020) 410–427. https://doi.org/10.1016/j.actbio.2020.02.017.
[48] T. Hanawa, and Y. Tsutsumi. Calcium phosphate formation on titanium and zirconium and its application to medical devices, Bioceramics Developments and Applications, 1 (2011).
[49] D.J. Blackwood, A.W.C. Chua, K.H.W. Seah, et al. Corrosion behaviour of porous titanium–graphite composites designed for surgical implants, Corrosion Science, 42 (3) (2000) 481–503. https://doi.org/10.1016/S0010-938X(99)00103-1.
[50] M. Najafizadeh, M. Ghasempour-Mouziraji, M. Hosseinzadeh, et al. Optimization of

biocorrosion resistance and mechanical properties of PM Ti–$_X$Al–2Fe–3Cu alloys by response surface methodology, Journal of Materials Science, 57 (2022) 18669–18686. https://doi.org/10.1007/s10853-022-07768-7.
[51] L. Liang, Q. Huang, H. Wu, et al. Stimulation of in vitro and in vivo osteogenesis by Ti–Mg alloys with the sustained-release function of magnesium ions, Colloids and Surfaces B: Biointerfaces, 197 (2021) 111360. https://doi.org/10.1016/j.colsurfb.2020.111360.